

Optimizing Logical Mappings for Quantum Low-Density Parity Check Codes

Sayam Sethi^{*†} 

Electrical and Computer Engineering
The University of Texas at Austin

Sahil Khan^{* }

Electrical and Computer Engineering
Duke University

Maxwell Poster^{}

Electrical and Computer Engineering
The University of Texas at Austin

Abhinav Anand^{}

Electrical and Computer Engineering
Duke University

Jonathan Mark Baker^{}

Electrical and Computer Engineering
The University of Texas at Austin

Abstract—Early demonstrations of fault tolerant quantum systems have paved the way for logical-level compilation. For fault-tolerant applications to succeed, execution must finish with a low total program error rate (i.e., a low program failure rate) relative to the baselines. In this work, we study a promising candidate for future fault-tolerant architectures with low spatial overhead: the Gross code (part of the Bivariate Bicycle code family [5], [31]). Compilation for the Gross code entails compiling to Pauli Based Computation and then reducing the pauli-based rotations and measurements to Bicycle instructions, including idling operations, in-module + inter-module measurements, and T -state preparation/injection. Depending on the configuration of modules and the placement of code modules on hardware, one can reduce the amount of resulting Bicycle instructions and improve compilation to produce a lower overall error rate.

We find that NISQ-based, and existing FTQC mappers are insufficient for mapping logical qubits on Gross code architectures because ① they do not account for the two-level nature of the logical qubit mapping problem, which separates into code modules with distinct measurements, and ② they naively account only for length two interactions, whereas Pauli-Product rotations are up to length n , where n is the number of logical qubits in the circuit. For these reasons, we introduce a two-stage pipeline that first uses hypergraph partitioning to create in-module mappings (clusters), and then executes a priority-based algorithm to efficiently assign clusters onto hardware. We find that our mapping policy reduces the error contribution from inter-module measurements, the largest source of error in the Gross Code, by up to $\sim 36\%$ in the best case, with an average reduction of $\sim 13\%$ relative to baselines. On average, we reduce the failure rates from inter-module measurements by $\sim 22\%$ with localized factory availability, and by $\sim 17\%$ on grid architectures, allowing hardware developers to be less constrained in developing scalable fault tolerant systems due to software driven reductions in program failure rates.

I. INTRODUCTION

Quantum computers have wide-ranging applications across a number of scientifically interesting problems, including factoring, optimization, and scientific simulations [9], [11],

[14], [24], [28]. The qubits used to perform computation are highly susceptible to errors; therefore, quantum error correction (QEC) must be implemented to ensure successful program execution. QEC codes use many noisy physical qubits to encode information into reliable *logical* qubits, enabling the construction of fault-tolerant architectures.

Current quantum computers are rapidly approaching the early fault tolerant era [1], [4], [23], [31], with demonstrations showing that noisy physical qubits can be used to achieve lower logical error rates. This transition is marked by significant progress across different hardware platforms, with proposals for systems featuring architectures with thousands of qubits [8], [21], and neutral atom platforms demonstrating support for up to 6000 physical qubits [19]. In this regime, the viability of a fault tolerant application is determined by its overall program error rate, and operational overhead is determined by the cost of performing *fault tolerant* primitives. These include syndrome extraction (performed between all operations to ensure that the physical qubits remain in the codespace), Clifford logical operations (which safely manipulate the *logical* state of the code with bounded error overhead), and on-Clifford T -state injections. Together, these operations form a universal fault tolerant gate set, and each QEC code provides its own methods for implementing these logical operations.

Recent proposals [30], [31] have increasingly focused on developing fault tolerant architectures around spatially efficient codes, which can encode more logical qubits per physical qubit, achieving a higher *encoding rate*. In particular, Bivariate Bicycle (BB) Codes [5], especially the Gross code [31], have been of interest due to their ability to achieve high distance (which determines the number of simultaneously correctable errors) while maintaining high encoding rate. The BB codes come with a fault tolerant architectural instruction set, known as the Bicycle Instructions, and several theoretical architectures based on the Gross code using the bicycle instruction set have significantly lower resource requirements compared to other early fault-tolerant proposals [12], [31].

^{*}denotes equal contribution

[†]sayams@utexas.edu

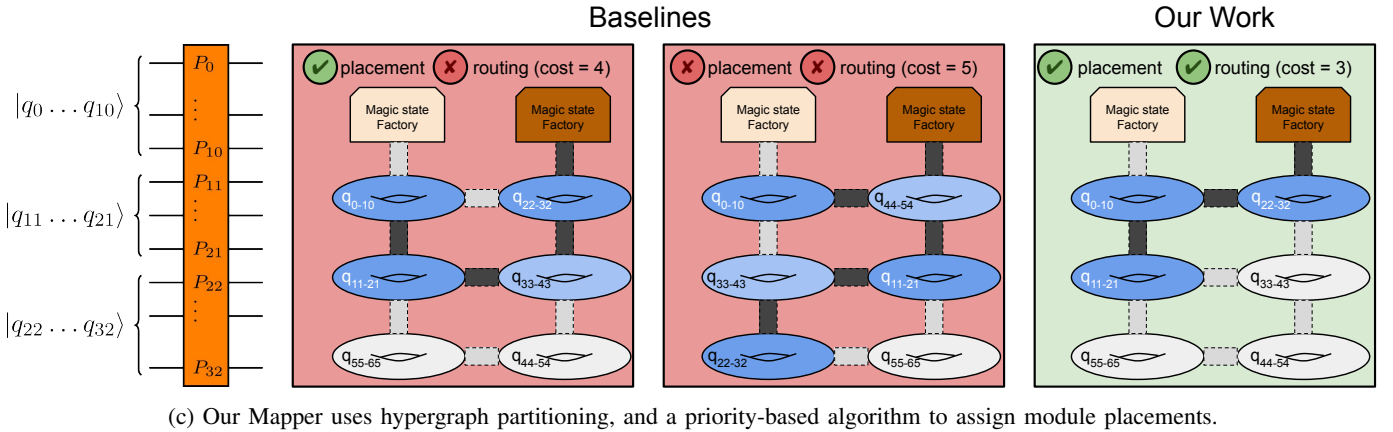
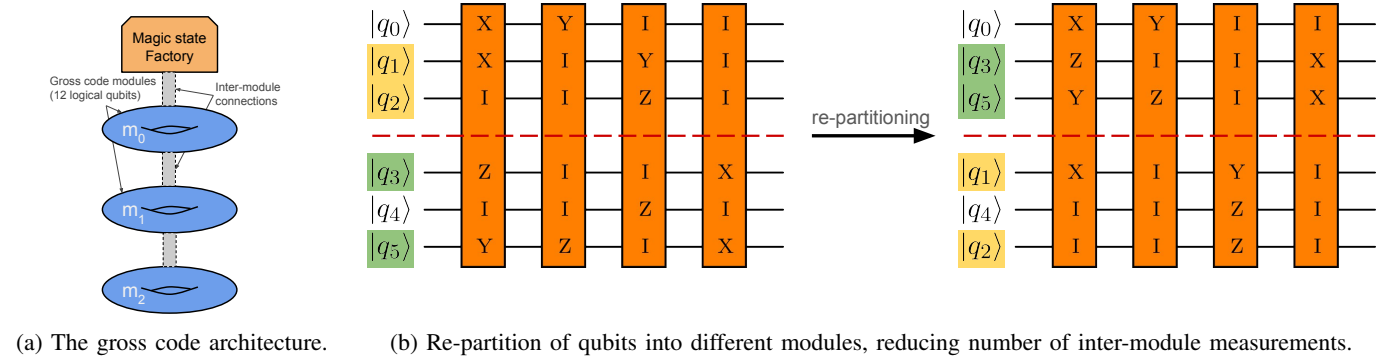


Fig. 1: **(a)** Three gross-code modules (12 qubits per module) connected linearly. Magic states are routed via inter-module connections to perform PRRs both within and across gross-code modules. **(b)** Qubits are initially divided into modules $\{q_0, q_1, q_2\}$ and $\{q_3, q_4, q_5\}$, requiring 4 inter-module interactions to complete the program. After re-partitioning into $\{q_0, q_3, q_5\}$ and $\{q_1, q_4, q_2\}$, the number of inter-module interactions reduces to only 1. **(c)** Our mapping policy compared to current state-of-the-art baselines. Dark blue modules contain qubits associated with the operation, while light blue modules are used only for routing to other modules. Either baselines perform adequate placement, but neglect routing, or vice versa, incurring substantial overhead by using more inter-module connections than required. Our mapping policy performs improved placement and routing to reduce the number of inter-module connections required to perform PRRs, significantly improving program success rate and reducing error accumulation.

These architectures assume that a given quantum circuit is first compiled according to the *Pauli Based Computing* (PBC) model, resulting in a list of Pauli Product Rotations (PPR) and Pauli Product Measurements (PPM). These are then translated into Bicycle Instructions, which include *idling operations* (syndrome extraction), *in-module* and *inter-module* measurements to address qubits within and across modules, respectively, and *T-state injections*. For an n -qubit Pauli product rotation, inter-module measurements are generated for every module on which the Pauli string acts trivially, while in-module measurements performed on each module handle the 11-qubit Pauli fragments corresponding to each block. Meanwhile, a T-factory runs separately at the edge of the line to generate T-states for Pauli product rotation of the form $R_z(\theta)$, and distributes them to the appropriate modules using inter module measurements from the cultivation and/or factory.

The Logical Qubit Mapping Problem Gross code blocks give the ability to configure both a module’s internal qubit layout and its relative placement on the device (assumed to be

either a line or grid due to hardware constraints [18], [31]). Changing this mapping directly affects the number of inter- and in-module measurements, as well as the distances between modules and the magic state factory, as seen in Figure 1c. Since each instruction contributes to the total error (or failure) rate of the program, the feasibility of running early fault-tolerant applications hinges on minimizing this total error budget. Our goal is therefore to generate mappings that reduce the total error contribution of these instructions.

Prior Work and Their Limitations Although this problem resembles the task of mapping physical qubits onto hardware in the noisy intermediate scale quantum (NISQ) era [2], [3], [20], [32], as well as mapping in FTQC [13], [29], existing solutions are inadequate for Gross-code logical mapping for the following reasons:

- 1) NISQ mappers model interactions only as length-2 operations, whereas PPR can involve up to n -logical qubits.
- 2) NISQ and FTQC mappers don’t capture the two-level structure of the mapping problem. Namely, the dis-

inction between *clustering* arbitrarily long interactions without the ability to route efficiently, and *assigning* modules to a linear topology in such a way where paths can be reused.

- 3) FTQC mappers assume that the cost of operations does not scale with the distance between the associated qubits, only requiring a routing path. Yet gross code operations are largely blocking, and their error costs scale with the distance between qubits/modules.

To overcome these limitations, we propose a first of its kind logical qubit mapper tailored for gross code architectures. Our mapping policy uses a two-step solution to address the in-module clustering problem and hardware assignment problem separately. First, our policy uses a hypergraph representation of length- n interactions and performs hypergraph partitioning to construct improved in-module mappings. This reduces the total number of inter-module measurements by up to $\sim 62\%$ in the best case, and by 20% on average. Next, the resulting clusters are mapped to hardware using a priority-based heuristic that considers certain activation patterns of inter-module measurements. This assignment is based on a logical-level connectivity graph. The approach used by our mapping policy is easily extensible to other BB codes, as well as other high-rate codes (i.e. codes with $k > 1$).

Furthermore, we perform sensitivity studies to compare our proposal’s efficacy on alternative topologies to the initial linear one proposed by [31] and under consideration by industry [18]. We also develop an improved path-finding algorithm for creating efficient inter-module measurement paths for grid topologies. We find that, across the dynamic part of compilation, we achieve over 40% reduction in program failure error rate in the best case, and a 17% reduction on average compared to the main baseline, SABRE [16], [32]. We also perform sensitivity studies of our proposal with variable factory availability and observe up to a $\sim 75\%$ reduction in program failure rate, with an average reduction of $\sim 23\%$ when each module has an associated factory. These are noticeable improvements that can bring hardware designers closer to fault tolerance without any hardware alterations.

Our contributions are as follows:

- 1) We show that NISQ mappers cannot effectively solve the logical qubit mapping problem on BB codes because of the two-level nature of the problem and the presence of n -qubit interactions. We introduce a two-stage algorithm that 1) performs hypergraph partitioning for up to n -qubit interactions and 2) executes a priority-based heuristic that encourages low-cost, repeated inter-module measurement patterns for hardware assignment.
- 2) We evaluate our algorithm on another realistic logical connection topology, the long-grid, and propose an efficient path-finding algorithm based on the topology.
- 3) We demonstrate that our mapping strategy reduces program failure rates by noticeable amounts, averaging $\sim 4\%$ at current estimates of error rates purely through software improvements, and noting relative reduction

will improve as devices get better, thereby easing hardware requirements for achieving scalable early fault tolerance.

II. BACKGROUND

A. Quantum Error Correction

Quantum computers are inherently noisy and this noise affects the accuracy, or fidelity, of quantum computations. Quantum Error Correction (QEC) is a technique that protects program execution from errors by adding redundancy to the encoded information. A quantum error correcting code (QECC) is defined by its code parameters $[[n, k, d]]$, where n is the number of physical qubits that are used to encode k logical qubits and d is the code distance. The code distance d is an important metric that determines the error-correcting capability of the code. A code of distance d can correct up to $\lfloor (d - 1)/2 \rfloor$ errors on distinct physical qubits. Another important metric of a QEC code is its encoding rate, which is defined as k/n . For the same distance, a QECC with a higher encoding rate is preferred over one with a lower rate, as it uses fewer physical qubits to encode the same number of logical qubits, thereby improving the space efficiency of the quantum computer. A prominent code family that satisfies these desirable properties is the class of quantum low-density parity-check (qLDPC) codes.

1) *Gross Code*: The gross code is a member of the family of the Bivariate Bicyclic codes, which is a subset of the qLDPC codes. The gross code has parameters $[[144, 12, 12]]$. Therefore, each logical block in the gross code consists of 144 physical qubits that encode 12 logical qubits, with a code distance of 12. Another variant of the code, the two-gross code, has code parameters of $[[288, 12, 18]]$. Both these codes are promising for large-scale fault-tolerant quantum computation (FTQC) due to their high encoding rates, and performing logical operations on gross (and two-gross) codes has been widely studied in literature [10], [25].

B. Measurement-Based/Pauli-Based Computation

Measurement-based quantum computing (MBQC) [7], [22] is a paradigm of quantum computation in which computation proceeds entirely via projective measurements and resource-state initialization Pauli-Based Computation (PBC) [6] is a specialized case of MBQC where the projective measurements are along arbitrary Pauli bases. To achieve universal quantum computation, PBC additionally requires access to a non-Clifford resource state which is typically either the $|T\rangle$ state ($= T|+\rangle$ state), or the $|m_\theta\rangle$ state ($= Rz(\theta)|+\rangle$ state). This paradigm is particularly attractive for architectures that do not natively support a universal gate set, or for QECC, such as the qLDPC code, for which a universal logical gate set is not yet known [31]. However, PBC introduces the challenge of reliably synthesizing magic states with high fidelities, to ensure that the overall quantum circuit executes with sufficiently high fidelities.

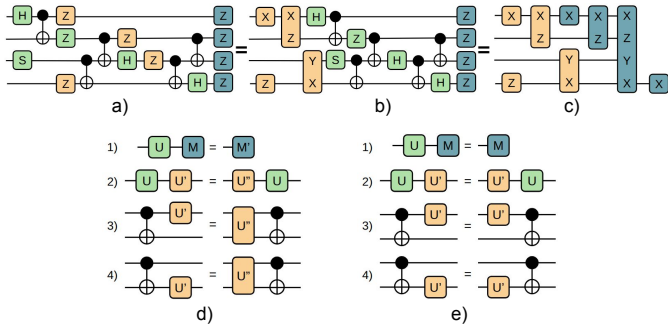


Fig. 2: A schematic illustrating the compilation of a circuit into its Pauli-Based Computation (PBC) form. (a) A circuit transpiled into H, S, CX, and T (or Rz) gates. Non-Clifford gates are shown in orange, Clifford gates in green, and measurements in blue. The anticommution rule (d) and commutation rule (e) (see Ref. [17] for details) are applied to systematically commute non-Clifford gates to the front, producing the intermediate representation in (b). Applying these rules to the measurements results in the fully translated PBC circuit in (c).

1) *Translating to PBC Circuits:* Recent works [17], [31] have proposed various compilation strategies for efficient translation from a gate-based circuit to a PBC circuit. These approaches start with a Clifford + T (or Rz) circuit. The Clifford gates in the circuit are first converted into Pauli measurements, which are then commuted across the non-Cliffords, modifying them as they commute through. At the end of the process, we are left with a sequence of Pauli product measurements. Each of these measurements requires a *magic state*, which is either a $|T\rangle$ or a $|m_\theta\rangle$ state. We demonstrate execution of the translation strategy, along with the commutation rules in Figure 2.

C. Tour de Gross Architecture

Tour de gross [31] is a compilation scheme proposed recently for executing universal, fault-tolerant operations for the gross code. Their proposed architecture consists of a single magic state factory at the top, followed by a line of gross code modules. Each module consists of 12 logical qubits, where the first logical qubit is used for routing and is called an ancilla (or a pivot, p_i) qubit. The other 11 qubits are used to store program qubits and are called logical program qubits. The tour de gross architecture supports 4 different kinds of operations, namely the shift automorphisms, in-module measurements, inter-module measurements and T injections. We list their properties in Table I. An illustration of translation of a circuit in the PBC model to the Bicycle instruction set is shown in Figure 3. Note that Compiling to $Rz(\theta)$ rotations in the Bicycle architecture results in PPRs of different widths than compiling directly to T .

1) *Quantum Program Execution:* Program execution on the tour de gross architecture proceeds as follows (also shown in

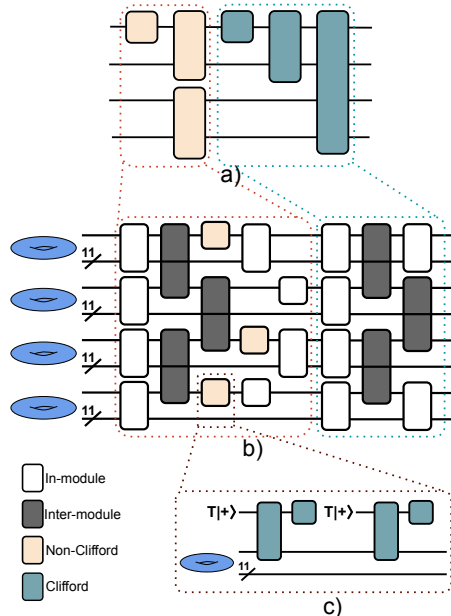


Fig. 3: Translation from a Pauli-Based Computation (PBC) circuit to the Gross-code Bicycle instruction set. (a) PBC circuit with Clifford measurements represented by blue boxes and non-Clifford measurements by orange boxes. (b) Resulting instruction sequence for execution on the Gross code, including in-module measurements (white boxes), inter-module measurements (grey boxes), and non-Clifford operations (orange boxes), the latter realized through T-state injection shown in (c). See Ref. [31] for further architectural details.

Instruction	Notation (i)	Timesteps	Logical error rate ($= P_i$)	
			$p = 10^{-3}$	$p = 10^{-4}$
idle	I	8	$10^{-8.8 \pm 0.2}$	$10^{-14.8 \pm 0.4}$
shift automorphism	U	14	$10^{-6.4 \pm 0.2}$	$10^{-12.2 \pm 0.5}$
in-module meas.	B	120	$10^{-5.0 \pm 0.1}$	$10^{-9.0 \pm 0.2}$
inter-module meas.	C	120	$10^{-2.7 \pm 0.1}$	$10^{-7.4 \pm 0.3}$
T injection	T	471	$10^{-5.5} + P_C$	$10^{-7.4} + P_C$

TABLE I: Bicycle instruction properties: Logical error rates and timestep durations at physical error rates $p = 10^{-3}$ and $p = 10^{-4}$. P_C is the logical error rate of inter-module measurements.

Figure 3). Consider an architecture with M modules laid out in a line, and a Pauli-based measurement $P(\varphi) = (P_{m_1} \otimes P_{m_2} \otimes \dots \otimes P_{m_M})(\varphi)$. Note that some of these M modules, say m_i , may not be involved in the measurement, and thus will have $P_i = 1^{\otimes 11}$. To execute $P(\varphi)$, a GHZ state is prepared via inter-module measurements on the pivot qubit. Within each module m_i , the entangled pivots then interact with the logical program qubits via in-module measurements to project the qubits along the P_{m_i} bases. Finally, the $|m_\varphi\rangle$ state prepared using the magic state factory and injections onto the pivot present in m_1 , the module closest to the factory.

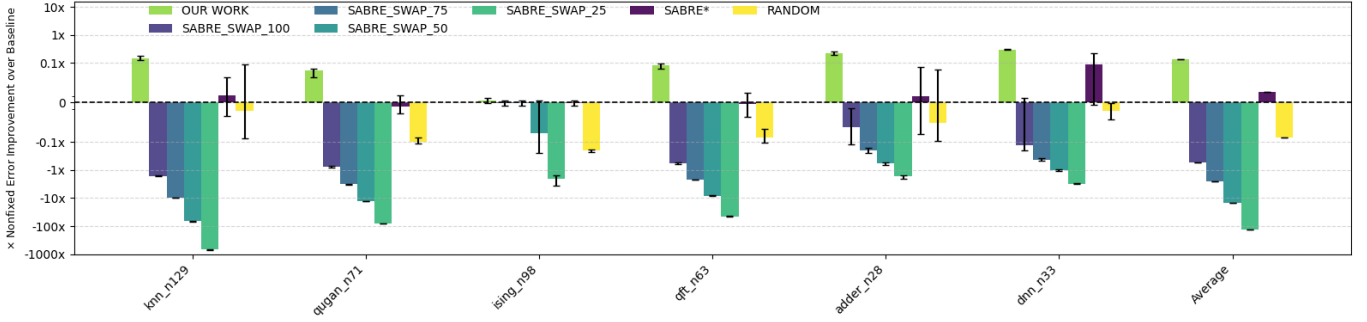


Fig. 4: A plot showing how SWAP insertion leads to a substantial increase in program error rate, contrary to NISQ compilation schemes. We evaluate the SABRESWAP strategy by inserting SWAPs every f rotations, and vary f between 25 and 100 rotations at intervals of 25 rotations. Smaller f leads to a much larger increase in inter-module measurements, which also makes it infeasible to simulate SABRESWAP strategies on all benchmark suites, or with a higher number of trials.

D. Qubit Mapping Problem

The problem of mapping program qubits onto the device has been widely studied in both the NISQ and FTQC regimes [2], [3], [13], [16], [32]. The NISQ-based approaches, such as SABRE [2], [3], [16], [32], solve the mapping problem by determining an initial qubit layout, and inserting SWAP gates to enable routing. However, as discussed in Section II-C, executing SWAP gates in PBC is expensive, and therefore, NISQ-based mapping approaches provide suboptimal layouts for execution. The algorithms used for NISQ-based mapping also scale poorly with an increase in the number of qubits and gate depths, making them unsuitable for large-scale FTQC circuit compilation. Moreover, NISQ-based compilation does not account for the location of magic-state distillation factories, which are located at the boundary of the logical device, as there is no notion of factories in NISQ-based computation.

The current state-of-the-art FTQC mapping approach [13], on the other hand, supports long-range gates, and therefore does not need to insert SWAP gates for routing. They instead attempt to maximize parallel execution of the long-range gates by partitioning the qubits into groups that can be operated on simultaneously. PBC compilation, and in particular, the tour-de-gross architecture, does not support parallel execution of Pauli-based measurements. Therefore, FTQC-based mapping approaches that aim to maximize parallelism do not work well for PBC architectures either.

The translation strategies discussed in Section II-B1 merely translate the input circuit into a PBC circuit and do not address the logical qubit mapping problem. Figure 1c shows how poor mappings can lead to increase in error rates and execution times. We discuss this in detail in Section IV-B.

III. IDENTIFYING CONSTRAINTS OF LOGICAL QUBIT MAPPING

In this section, we explore how different measurement types are affected by a logical qubit mapping. We first show that neither SWAP insertion nor in-module measurement substantially improve error rates. We also demonstrate that the majority of

the program error (failure) is dominated by fixed, synthesis-based, inter-module cost, and conclude that the most effective strategy for reducing program error (failure) minimizing the non-synthesis-based inter-module measurements. We explore two methods to reduce inter-module measurements, and later use these principles to build our mapping policy.

A. Routing via SWAP Insertion is Impractical

We can execute a Pauli measurement on qubits q_A, q_B in modules m_i, m_j by first swapping q_A with another logical qubit in m_j , or swapping q_B with another logical qubit in m_i . We can then execute the target Pauli measurement via a sequence of in-module measurements. In either case, we will need to execute 3 CNOT gates that act on q_A, q_B . Each CNOT gate requires entangling modules m_i, m_j , and all the modules that are present between the two. Therefore, if m_i, m_j are x modules apart, this introduces $3x$ inter-module measurements. Additionally, a sequence of in-module measurements in m_i (or m_j) would be required to execute the Pauli measurement between q_A, q_B . Say, this requires y in-module measurements. Since P_C, P_B are small, we can compute the total error as $\varepsilon_{\text{SWAP}} \approx 3xP_C + yP_B$. We require $120 \cdot (3x + y)$ timesteps using the SWAP insertion approach.

On the other hand, if we would have directly entangled the two modules m_i, m_j via x inter-module measurements, followed by in-module measurements within both m_i and m_j . This requires only x inter-module measurements and $y_i + y_j$ in-module measurements. The error of this method of execution is $\varepsilon_{\text{inter}} \approx xP_C + (y_i + y_j)P_B$. This approach requires $120 \cdot (x + \max(y_i, y_j))$ timesteps.

Therefore, as long as $\max(y_i, y_j) - y < 2x$, this approach is faster than the version via SWAP insertion. Since in the tour-de-gross ISA, over 90% of the in-module sequences are close to the mean [31], the difference will be very close to 0, and the inequality holds. Additionally, since P_C is 2 orders of magnitude larger than P_B (Table I), and $y, y_i, y_j \in [1, 25]$, for any x (distance between the modules), we will always have $\varepsilon_{\text{inter}} \ll \varepsilon_{\text{SWAP}}$. Therefore, routing logical qubits through SWAP operations is always inferior for the tour-de-gross ISA.

We also estimate the effects of SWAP insertion to remap the grid with changing frequencies. In Figure 4, we insert SWAPS at varying frequencies via the SABRESWAP heuristic. We observe that, regardless of SWAP insertion frequency, the program error rates, and equivalently the total number of inter-module measurements worsen by 1-2 orders of magnitude.

B. In-Module Measurements are not the Bottleneck

A mapping fixes blocks of 11 logical qubits within each module for the logical computation, which entails compiling a list of PPRs R that make up the entire circuit. A single n -qubit rotation r is spread across M modules and the rotation corresponding to a module m is denoted as $B_{m,r}$. Therefore, the total in module measurement cost, C_{in} , is

$$C_{in} = \sum_r \sum_m T(B_{m,r})$$

where T is the cost associated with the rotation from the lookup table of optimal Clifford synthesis in Ref. [31]. The cost range from 1-25 in-module measurements, with an average of 18.5 measurements.

1) *Contrived Case*: In Figure 5, we show a contrived example where mapping drastically changes the in-module measurement cost for a single rotation. A naive mapping leads to a synthesis of 5 rotations for the top module and 7 rotations for the bottom module, leading to 12 total in-module measurements required for the entire rotation. However, in a mapping that is aware of the costs of Clifford synthesis, one can re-partition the qubits and perform this rotation with only 2 in-module measurements, as both of these rotations are native measurements to the BB code.

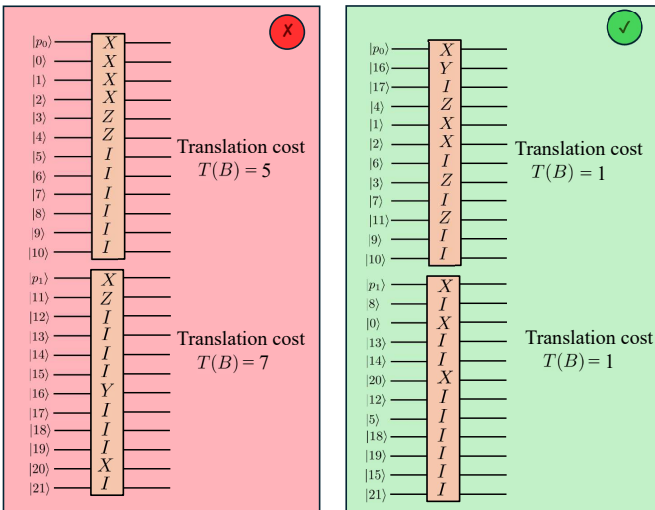


Fig. 5: A figure illustrating the effect of logical-qubit remapping on in-module measurement cost. Left: A naive mapping leads to higher cost. Right: A mapping exploiting the in-module measurement Clifford table leads to significantly reduced cost.

2) *Realistic Scenario*: In practice, a circuit is not just one rotation but a list of rotations, of large depth (up to tens of thousands). Once a mapping is assigned, it must serve as a *global solution* across all rotations, since inserting SWAP gates is sub-optimal as discussed in Section III-A. However, as the number of rotations increases, the in-module measurement synthesis cost per rotation converges toward the average of 18.5, and over 90% of the measurements require 19 ± 6 in-module measurements [31]. Experimentally we observe that the in-module measurement errors lag behind inter-module errors by about one order of magnitude, as seen in Figure 6. This is because given the error model from Table I the ratio of in-module to inter-module error rates is $\approx 1:100$, and since we have 18.5 in-module measurements for every inter-module measurement, we see approximately one order of magnitude lag behind.

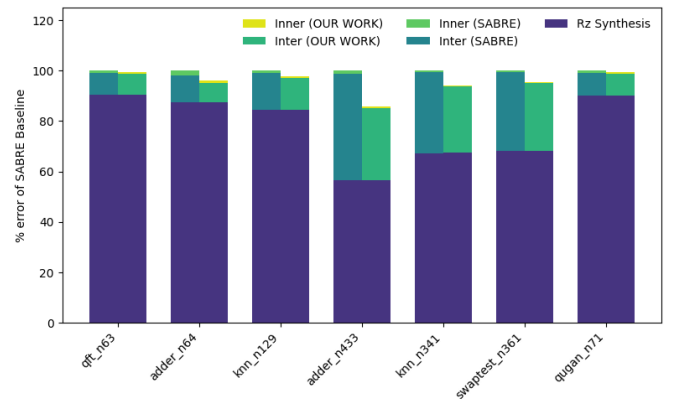


Fig. 6: Breakdown of total program error contributions across different error sources for a range of benchmarks.

Even in an idealized scenario where an in-module measurement could be traded for an inter-module measurement, Figure 7 shows that inter-module measurements remain far more expensive. For example, the worst-case in-module cost of $25 + 25 = 50$ and one inter-module measurement still has a lower error rate than $1 + 1 + 1 = 3$ in-module and 2 inter-module measurements. Therefore, optimizing in-module measurements provides little advantage, and we shift our focus on reducing the inter-module measurements.

C. Inter-Module Measurements can be Minimized via Partitioning

Different logical mappings can also vary the number of inter-module measurements, which are the most expensive bicycle instruction in terms of error contribution (as seen from Table I and Figure 6). Notably, we distinguish between the fixed amount of synthesis-based inter-module measurements, which are needed for each benchmark, and the non-fixed, or *optimizable*, inter-module measurements which are mapping/compilation dependent. We can reduce the number of non-synthesis-based inter-module measurements through mapping due to two reasons.

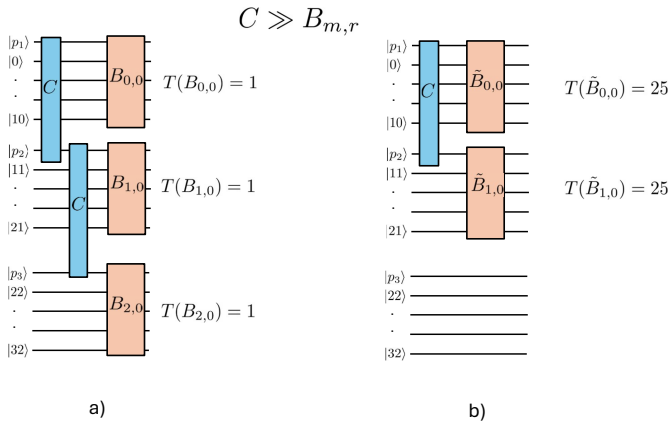


Fig. 7: Inter-module measurements (C) are much more expensive than in-module measurements ($B_{m,r}$), such that saving just one inter-module measurement part (b) is worth the cost of having the worst case in translation for in-module measurements (a)

1) *Creating Trivial In-module Measurements:* A given rotation may have a span of 12 bits $i_1 \dots i_{12}$ of all identities inside a single module, producing a trivial in-module rotation. This avoids both in-module and inter-module measurements. Mappings that align identity blocks with module boundaries can therefore reduce inter-module operations across all rotations.

2) *Finding Efficient Paths to the Factory:* For each rotation, a T-state is generated at the factory and must propagate to the required modules using inter-module measurements. In a linear topology (see Figure 1a), this propagation requires the T-state to traverse each intermediate module sequentially to reach the farthest target module. However, by leveraging trivial in-module measurements (Section III-C1), a rotation may involve anywhere from 1 module to M modules, rather than always involving all M modules. Thus, the physical placement of modules relative to the factory directly impacts the number of inter-module measurements, and therefore the overall program error rate. Consequently, the inter-module measurement cost for a rotation is equal to the number of edges in the minimum spanning tree that connects the factory and all modules participating in that rotation.

IV. OUR PROPOSAL: ENHANCED LOGICAL MAPPING

Using the insights developed in Section III-C, we aim to reduce the *inter-module measurements* using the two methods discussed in Sections III-C1 and III-C2. We find that each of these problems requires tailored heuristics to solve the respective clustering and assignment problems individually. We define the problem of reducing nontrivial inter-module measurements and finding efficient paths to the factory as the *clustering* and the *assignment* problem, respectively. As a result, we propose a two step approach that solves both of these problems. We first focus on reducing inter-module measurements by using a hypergraph partitioning to re-partition the circuit by constructing clusters that minimize the number

of modules involved in each rotation, thereby reducing the number of non-trivial modules involved in each rotation. Secondly, we use the partitioned clusters to make assignments to physical locations based on the ability to recycle repeated paths of certain sets of module(s), thereby minimizing the total inter-module cost for the chosen clustering.

A. Efficient Clustering via Hypergraph Partitioning

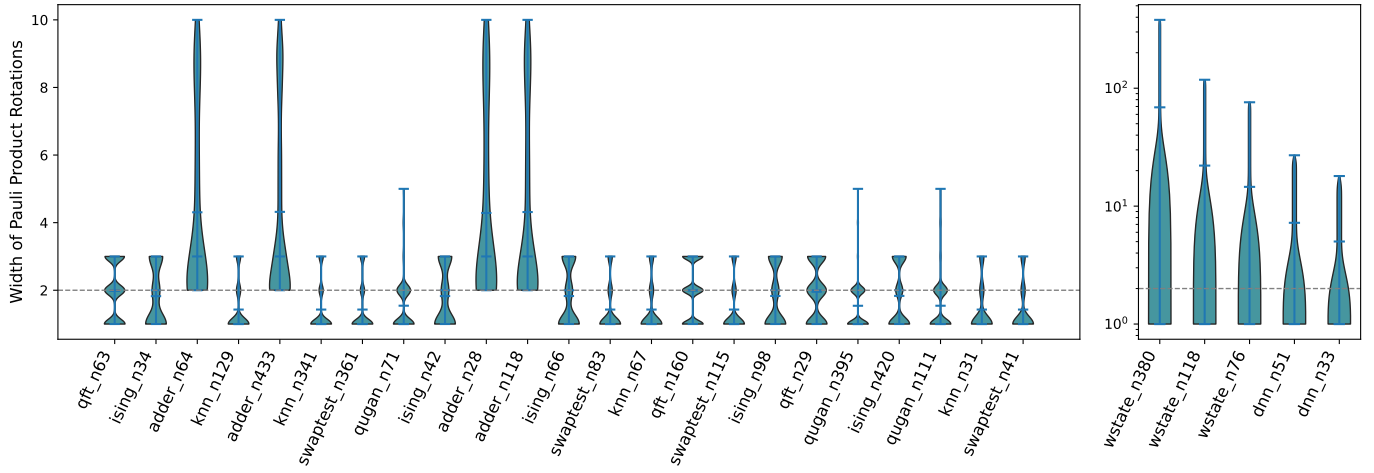
To construct clusters of logical qubits that should be grouped within a module, we represent each interaction in a given rotation as an edge in a hypergraph, where an edge can span more than 2 nodes. We assign weights to these hyperedges using the frequency of the rotation, i.e., if a certain rotation is executed multiple times in any permutation. This is essential, as Figure 8a shows that every benchmark has rotations of width > 2 . The optimization problem is to then partition the graph into M cuts such that the weight across each of the cuts are minimized, creating clusters of size up to 11, where qubits that interact frequently are in the same group.

We use KaHyPar [26], [27] with ε value at 0.06 to implement this partitioning. Creating clusters using KaHyPar reduces the number of modules involved in each rotation, allowing for more possible trivial inter-module measurements. We compare against SABRE, SABRE*, as well as METIS in Figure 10 wherein we show a toy example such that the hypergraph partitioner generates a partition that reduces the inter-module cost. Across all benchmarks, we report the reduction in number of non-trivial inter-module measurements outputted by KaHyPar in Figure 9.

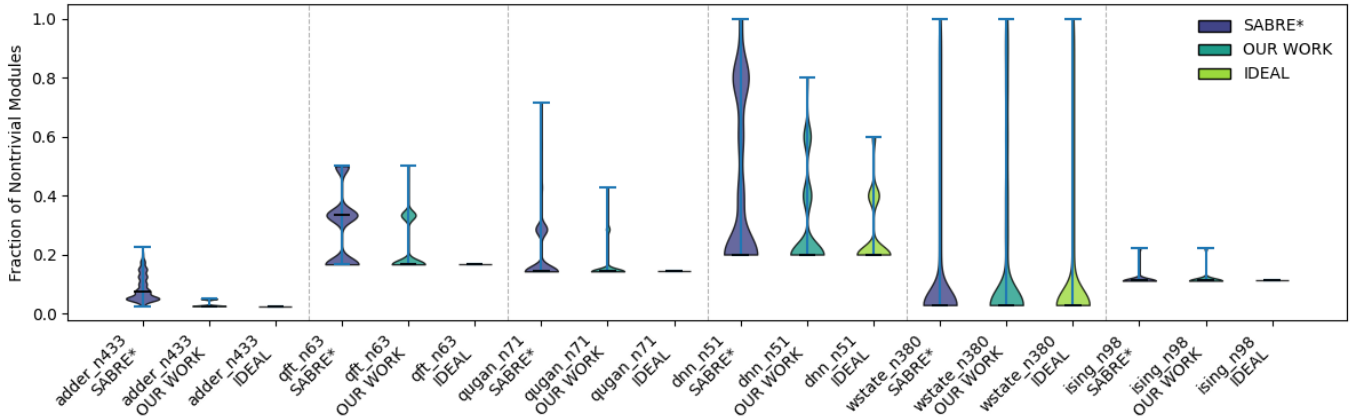
Figure 8b also shows how our mapper is able to minimize the number of nontrivial rotations, shifting the distribution of nontrivial modules on a per-rotation basis. We find that, apart from wstate and ising, KaHyPar is able to reduce the number of inter-module measurements compared to SABRE*. These benchmarks offer no scope for efficient partitioning since both of them have all-to-all qubit interactions, wstate in the form of large weight interactions that span all modules, and ising in the form of all qubit combinations of low-weight interactions. This is also reflected in Figure 9, where the improvement from our mapper is significant on all benchmarks classes except these two. Furthermore, it performs best on benchmarks which have rotations with higher density of widths that are > 2 , but do not span the entire width of the program. Overall, Figure 14 demonstrates that hypergraph-partitioning-based clustering strategies, when coupled with any of the assignment policies, consistently reduce the resulting error.

B. A Priority Based Algorithm for Efficient Assignment

Finding efficient paths to the factory must leverage the ability to assign module locations such that common paths are reused. Moreover, if a module is involved in fewer rotations, it will likely have a smaller contribution to the inter-module measurement cost, and thus the overall error rate. Such modules should be placed further away from the factory. Inspired from these observations, we propose the priority heuristic described



(a) Distribution of PPRs length across representative QASMBench [15] Benchmarks. Notably, all benchmark contains non-trivial interactions of width > 2 . On the right we separated out benchmarks with larger with rotations and used logscale.



(b) Comparing the fraction of modules used for a Pauli Product Rotation after partitioning, between our mapping policy, SABRE* and the ideal case (i.e., $\lceil \frac{n}{11} \rceil$, where n qubits are involved in the rotation).

Fig. 8: Comparing the width of the Pauli Product Rotations before and after partitioning.

Algorithm 1 Priority Assignment Heuristic

```

1: procedure ASSIGNPRIORITIES(Rotations, numModules)
2:   Priorities  $\leftarrow \{\}$ 
3:   priority  $\leftarrow 0$ 
4:   modules  $\leftarrow \{(id: modID, freq: 0, rotations: \emptyset) \mid modID \in [1, numModules]\}$ 
    $\triangleright$  initialize a list of modules with frequencies
5:   for all rotation  $\in$  Rotations do
6:     for all module  $\in$  rotation do
7:       modules[module].freq  $\leftarrow$  freq + rotation.freq
8:       modules[module].rotations  $\leftarrow$  modules[module].rotations  $\cup$  rotation
    $\triangleright$  update the frequency of module and add rotation
9:   while modules  $\neq \emptyset$  do
10:    module  $\leftarrow$  GETMODULEWITHLEASTFREQ(modules)
11:    modules  $\leftarrow$  REMOVEMODULE(modules, module)
12:    modules  $\leftarrow$  DELROTATIONANDFREQUENCIES(modules, module.rotations)
    $\triangleright$  delete the rotations and frequencies associated with module
13:    Priorities  $\leftarrow$  Priorities  $\cup$  (module.id, priority)
14:    priority  $\leftarrow$  priority + 1
15:   return Priorities
    $\triangleright$  returns a dictionary of (moduleID, priority) pairs

```

in in Algorithm 1. One of the key insights of our heuristic lies in the observation from Figure 11, wherein we note that for a linear architecture, the cost of the rotation is solely

determined by the placement of the non-trivial module that is the furthest away from the factory. This insight holds true even for a grid architecture with a limited number of factories. Routing to modules on grids with a constant width involves limited interactions along the rows and most of the inter-module cost comes from routing along the columns. We detail this discussion in Section IV-C.

Our heuristic counts the number of rotations each module is involved in, and starts assigning priorities outside in, that is, it first identified modules with the least frequencies and assigns it the least possible priority. It then removes all rotations that are incident on this module, We also update the frequencies of the other modules that are involved in the removed rotations, since the remaining unassigned modules do not affect the inter-module cost of such rotations anymore. We repeat the above algorithm until there are no more modules left to be assigned.

We compare the difference between hypergraph partitioning with a greedy assignment heuristic versus our priority heuristic

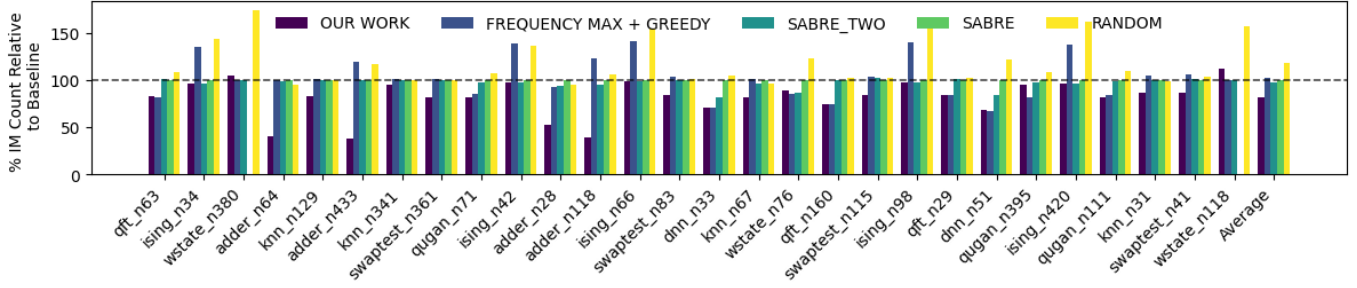


Fig. 9: Relative reduction in the number of inter-module measurements achieved as percent improvement over SABRE.

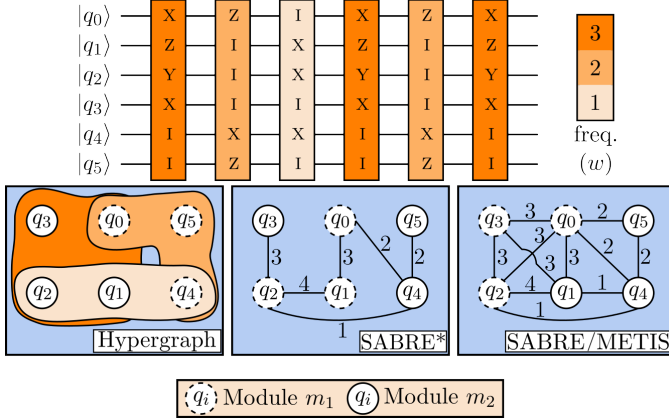
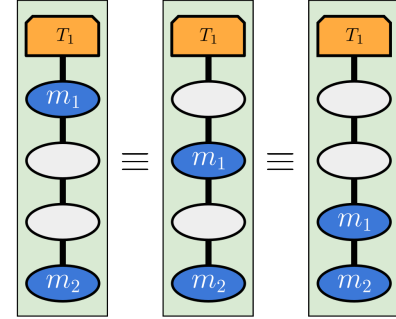


Fig. 10: Example of a PBC circuit partitioned using four methods: hypergraph (left), SABRE (middle), and SABRE*/METIS (right). Each Pauli-layer involves nontrivial operations on multiple qubits (frequency of repetition are indicated by the color gradient). Each method builds an interaction graph weighted by the number of interactions each qubit has with each other. The hypergraph appends a frequency-weighted (hyper)edge for each operation, SABRE* adds linear edges per operation, and SABRE*/METIS add a quadratic number of edges for each operation. Qubits are then partitioned into modules by computing min-cuts.

to better see an isolation of variables. We also compare all policies against each other and we report the performance across all benchmarks in Figures 14. We also show the improvements gained by implementing Algorithm 1 on top of baseline mapping strategies in Figure 12.

1) *Optimality of Algorithm 1:* We prove the optimality of the placement heuristic for the case of a line architecture and a single factory at the end of the line. The same proof idea extends to a grid architecture and the multiple factories case. For simplicity, we assume that all modules have distinct frequencies as computed in Algorithm 1. This guarantees that the optimal priority assignment is unique. Let the optimal priority assignment be denoted by \mathcal{M}^* . Furthermore, let the assignment returned by Algorithm 1 be denoted by \mathcal{M} , and assume that $\mathcal{M} \neq \mathcal{M}^*$. We will now show that this leads to a contradiction, and therefore, the assignment given by



Intermodule Measurement Cost: 4

Fig. 11: Regardless of module placement for m_1 the intermodule cost is always 4, as m_2 was placed 4 modules away, ultimately requiring 4 inter-module connections between the magic state factory and m_2 .

Algorithm 1 is optimal and equal to \mathcal{M}^* . Since we assumed $\mathcal{M} \neq \mathcal{M}^*$, there exists some priority on which \mathcal{M} and \mathcal{M}^* differ. Consider the smallest such priority i , and let the module assignment by $\mathcal{M}, \mathcal{M}^*$ at priority i be m_i, m_i^* respectively, where $m_i \neq m_i^*$. Since we assumed all modules have distinct frequencies, and Algorithm 1 chooses module m_i such that it has the least frequency, we have $F(m_i^*) > F(m_i)$, where $F(\cdot)$ is the frequency function. Therefore, the cost of inter-module rotations after the i^{th} assignment can be computed as (using the approach from Figure 11),

$$\begin{aligned} \text{cost}_i(\mathcal{M}) &= \text{cost}_{i-1}(\mathcal{M}) + F(m_i) \cdot (n_m - i) \\ &= \text{cost}_{i-1}(\mathcal{M}^*) + F(m_i) \cdot (n_m - i) \\ &< \text{cost}_{i-1}(\mathcal{M}^*) + F(m_i^*) \cdot (n_m - i) < \text{cost}_i(\mathcal{M}^*), \end{aligned}$$

where in the second step we used the fact that the assignments were identical up to step $i - 1$, and n_m is the number of modules. Since we have that Algorithm 1 achieves a lower cost than the optimal assignment, it could not have been the case that m_i differs from m_i^* , which leads to a contradiction.

C. Routing on Grid Topologies

Although the tour de gross architecture assumes a linear connection topology between the modules and the factory, we also evaluate our mapper on a more realistic topology that researchers are currently investigating for fault-tolerant

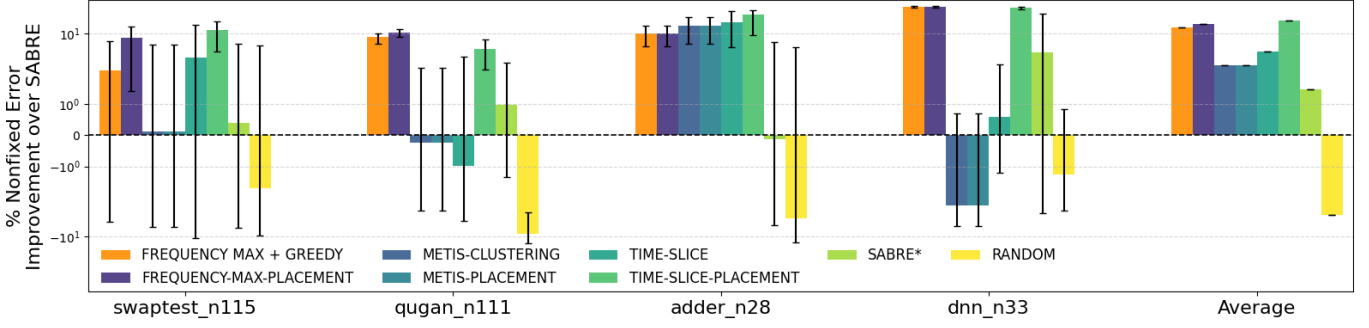


Fig. 12: We demonstrate program error rate improvements obtained from using Algorithm 1 in conjunction with different partitioning policies. Algorithm 1 enhances the improvements obtained by each partitioning strategy. Note that the average reported is over the depicted subset of benchmarks and not the entire benchmark suite used in Section V.

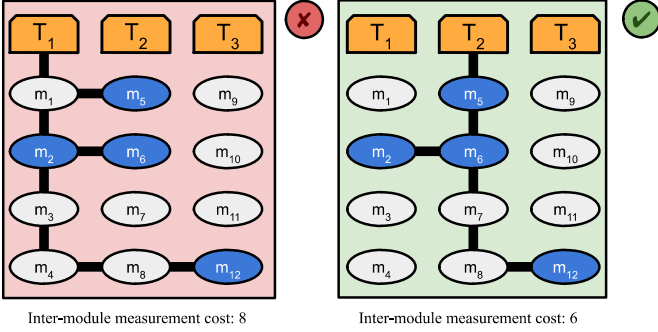


Fig. 13: An example of the path-finding algorithm on the long-grid topology, where three T-state factories T_1, T_2, T_3 are positioned along the short edge of the grid.

architectures [18]. Since the circuit execution in the four de gross ISA is largely sequential, and each module consists of 11 logical data qubits, we only have 40 modules for the largest benchmark. In addition to this, the factories are no longer the bottlenecks in terms of execution times (Table I) of the gates. Therefore, we consider factories that are arranged along the short edge of a *long-grid*, where the grid’s length is significantly larger than its width. For a grid with M modules and f factories, where $f \ll M$, we can define the dimensions of the grid as $\lceil M/f \rceil \times f$ and treat f as a constant.

Even on such *long-grids*, brute-forcing the optimal path that minimizes the inter-module cost requires searching an exponential space. Therefore, we propose a fast path-finding approach that is nearly optimal for such topologies. We find that since the grid is much longer than it is wide, and T-state must originate from a single factory, it is more effective to explore depth-wise along the long dimension from the central factory and branch out horizontally only when necessary. We demonstrate this in Figure 13, where we explore length-wise to the maximum required depth while ensuring that the horizontal (width-wise) movement incurs minimal inter-module measurements, while still achieving the optimal depth-wise cost. Since we have a constant number of factories in a

long-grid, we can perform this search for each possible factory as a starting point and choose the one which minimizes the inter-module cost.

V. EVALUATION AND METHODOLOGY

A. Generalized Method

We first compile benchmarks from QASMBench [15] to obtain our logical circuit benchmarks. These circuits are then translated to a Pauli-based computing model following the commutation rules discussed in [17], [31] (Figures 2, 3), such that each circuit is represented as a list of PPR. Given a benchmark of n -logical qubits, the number of Gross-code modules is $M = \lceil \frac{n}{11} \rceil$. Each mapping policy takes the rotation list and the number of modules as input, and outputs a mapping from the logical qubit to the module. Once a mapping is produced, we decompose each rotation into a set of 11-qubit Pauli-blocks at each timestep. Each rotation, $P(\varphi) = (P_{m_1} \otimes P_{m_2} \otimes \dots \otimes P_{m_M})(\varphi)$, is annotated with a set of modules, $\mathcal{M} = \{m_i \mid P_i \neq I^{\otimes 11}\}$ which represents the non-trivial modules involved in that rotation. In the case of a linear topology, the optimal path is the path that connects module $\max(\mathcal{M})$ to the factory, i.e., the module that is the furthest away from the factory. Using this path, we calculate the number of inter-module measurements needed for a given rotation, and we use the table provided in [31] to get the in-module measurement cost upon each of the $|\mathcal{M}|$ modules participating in a nontrivial rotation. The total program failure rate (P_{total}) is calculated based on the complement of the success probability:

$$P_{\text{total}} = 1 - \prod_{\text{operation}_i \in L} (1 - p_{\text{operation}})$$

where L denotes all the bicycle instructions in the circuit, and $p_{\text{operation}}$ is obtained from Table I. Note that the total program failure rate corresponds directly to application performance. In practice, the confidence level for an application is given by the product of the number of shots of the application and the success probability. We can expect an application to be run with $\# \text{ shots} \cdot (1 - P_{\text{total}})^{-1} \approx \# \text{ shots} \cdot (1 + P_{\text{total}})$ (this approximation holds in the FTQC regime where failure rates

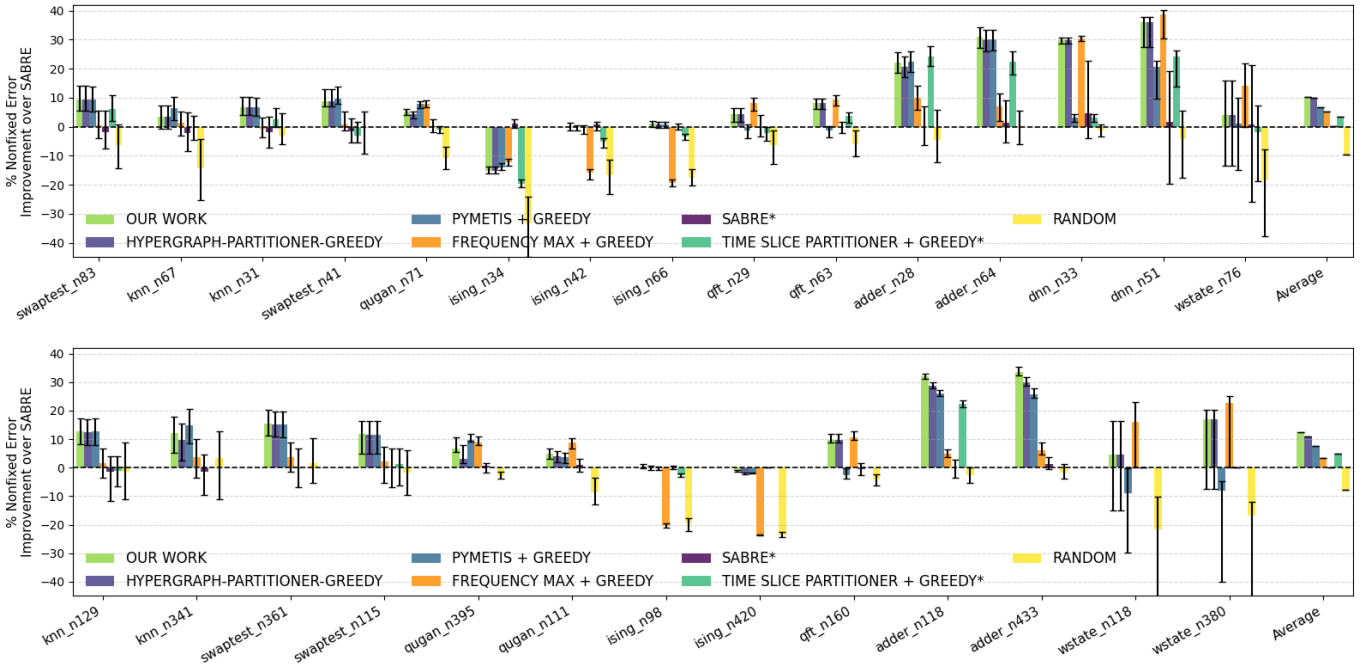


Fig. 14: Results for medium-sized (top) and large-sized benchmarks (bottom) from the QASMBENCH suite [15], showing relative percentage improvements in program error rates of our mapper over baseline compared to SABRE, SABRE*, Time Slice Partitioning*, and METIS on the non-fixed/optimizable portion of the compilation.

are small). Therefore, an improvement of $c\%$ in total program failure rate corresponds to a $c\%$ improvement in application wall time, or, a $c\%$ improvement on the depth of a given circuit for the same execution time. We assume the physical error rates of all bicycle instruction to be $p = 10^{-4}$. The synthesis cost is calculated with a precision of 10^{-4} , giving ~ 40 T gates (Cliffords are commuted to the end of the circuit). Each synthesized T gate requires an additional inter-module measurement with the module adjacent to the factory (as shown in Figure 3).

B. Baselines

Since the logical qubit mapping for Bivariate Bicycle (BB) codes lacks previous standardized methodologies, we evaluate five different baseline strategies throughout the paper. Some of these, such as SABRE [16], time-slice [2], and METIS [13], are adapted from NISQ-based and FTQC-based mappers, and the remaining baselines rely on naive heuristics designed specifically for the logical-module setting. For each baseline we consider both the *clustering* heuristic to partition qubits into modules, and the *assignment* heuristic to assign the modules to a physical location. Due to nondeterminism in several baselines, we perform 10 independent runs and report mean values with error bars. We also report the mean and standard deviation for the compilation time taken by each mapping policy in Table II. These were computed on a Lenovo machine with Intel Ultra 9 185H and 64 GB of RAM.

1) *NISQ-Based and FTQC-Based Baselines*: Four of our baselines are inspired from state of the art NISQ mappers,

Policy	Mean (s)	Std (s)	#Timeouts
RANDOM	1.71	3.45	0
FREQUENCY MAX + GREEDY	2.11	4.25	0
Our Mapping Policy	2.61	5.54	0
HYPERGRAPH-PARTITIONER-GREEDY	2.62	5.31	0
METIS-CLUSTERING	3.23	5.89	0
SABRE*	4.37	8.93	0
SABRE	5.19	11.89	2
TIME-SLICE	75.14	93.55	10

TABLE II: Runtime statistics (mean and standard deviation) across benchmarks sorted by mean. Timeouts correspond to runs that took longer than 5 minutes.

which we adapted for the bicycle code logical qubit mapping problem: SABRE, SABRE* [16], Time Slice Partitioning* [2] and METIS [13]. Since the NISQ baselines do not consider k -qubit interactions (for $k > 2$), we model the rotations as 2 versions of each NISQ baseline: one version where CXs are all to all connected between a length k interaction, and one version where a single CX connects the length k interaction in a single linear chain. On programs with n qubits, the first approach generates graphs with $O(n^2)$ edges, whereas the latter approach generates graphs with only $O(n)$ edges. However, the first approach has the advantage of capturing all possible orderings of qubits, whereas the second approach is faster. Indeed we see that the all-to-all variants exhibit severe computational overhead and frequently encounter timeouts or memory exhaustion. For this reason, SABRE has missing data points for certain benchmarks, and the all-to-all variant of Time Slice Partitioning was discarded entirely. We denote the

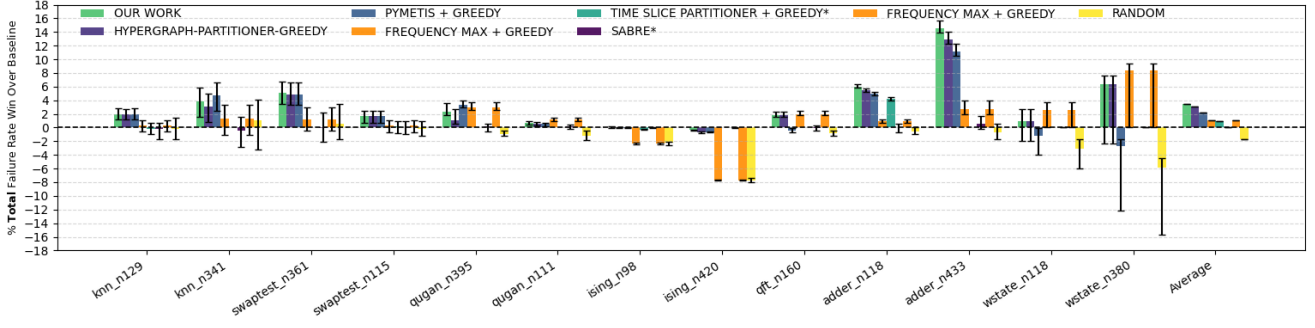


Fig. 15: Including the fixed T-synthesis error, we report the total program failure rate expressed as a percentage relative to the baseline, SABRE. Relative percentage improvement over SABRE is shown for each mapper.

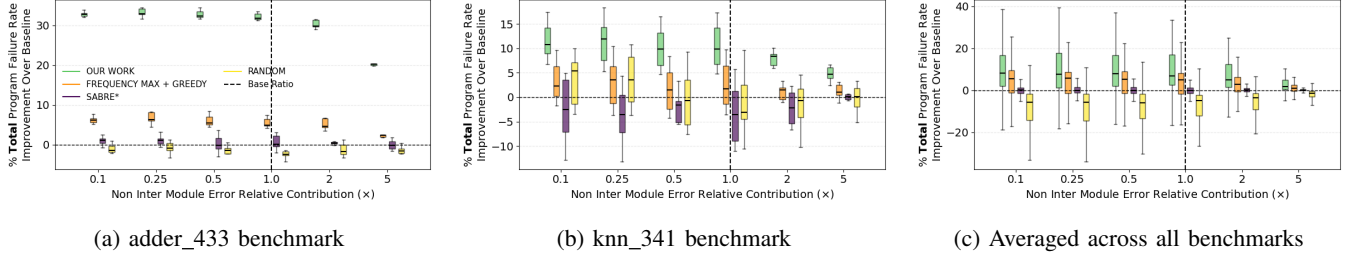


Fig. 16: Sensitivity to the Rz Synthesis Error contribution (note that this plot assumes $P_C = 0$ only for injections since injection error rates have not been determined in literature for arbitrary extractor architecture).

latter version of each baseline with a star. Even Time Slice Partitioning* occasionally fails to complete on the linear chain connectivity.

Due to this inconsistency, SABRE serves as our *primary NISQ baseline*, with SABRE* used only when SABRE itself times out. We pass to SABRE a line connectivity graph of all logical qubits, since SABRE does not have the ability to consider modules/module connectivity, and we assume that all qubits i , where $\lceil \frac{i}{11} \rceil = k$ are grouped together into module m_k from the output line to artificially make the clusters. Time Slice Partitioning in contrast, can explicitly model cluster structure, given the device graph and the number of partitions $\lceil \frac{n}{11} \rceil$ of size at most 11. However, it does not address the problem of relative orderings of these modules. We therefore use a greedy assignment policy, placing the most frequently used module (as determined by the partition policy) closest to the factory.

2) *Customized Greedy Baseline*: We also use our own naive heuristic to serve as a baseline that was purposed for the logical qubit mapping problem, we call “frequency maximizing” clustering. This counts the frequencies of each logical qubit being involved non-trivially in a rotation, and creates a list in descending order from most used to least used logical qubits. The policy then assigns qubit q_i at index i in the list into module m_k , where $k = \lceil \frac{i}{11} \rceil$. We combine this with the same greedy assignment heuristic, as in the case of Time Slice Partitioning policy, where the most used modules are physically assigned to locations closest to the factory.

C. Evaluation on Non-fixed Error vs Total Error

Referring to the analysis in Section III-C, placement and routing cannot address the overheads associated with the Rz state synthesis and the ensuing inter-module measurements required to inject T-states into the module for executing rotations. Additionally, these operations take up a majority of the total failure probability (P_{error} as defined in Section V-A), and cannot be altered by using different mapping policies. As a result, we also compare the contribution to the total failure probability from the in-module and inter-module operations, i.e., the mapping-dependent failure probability (which we call the non-fixed error, or $P_{\text{non-fixed}}$). We report the errors for $P_{\text{non-fixed}}$ in Figure 14 and the errors for P_{total} in Figure 15.

D. Sensitivity Analysis

1) *Sensitivity to the Rz Synthesis Error Contribution*: We show how the improvement in total failure probability (P_{error}) of our policy and other baselines changes depending on the relative contribution of errors from sources other than the inter-module measurements in Figure 16. The error rates used from Table I are estimates by IBM based on current and projected quantum device capabilities [31], and correspond to a contribution of $1\times$, which is depicted by the *base rate* line. However, different devices such as neutral atoms, trapped ions, improvements in quantum hardware, etc., as well as arbitrary extractor architectures, will change the relative error landscape between these operations. As advances are made, the Rz synthesis error rates will reduce and therefore, FTQC architectures will shift to a regime corresponding to relative

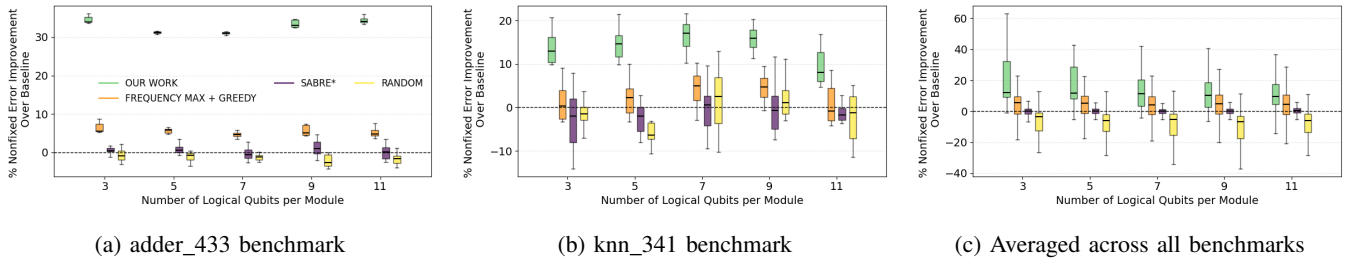


Fig. 17: Exploring different amounts of logical qubit numbers per module and the effect on non-fixed error improvement.

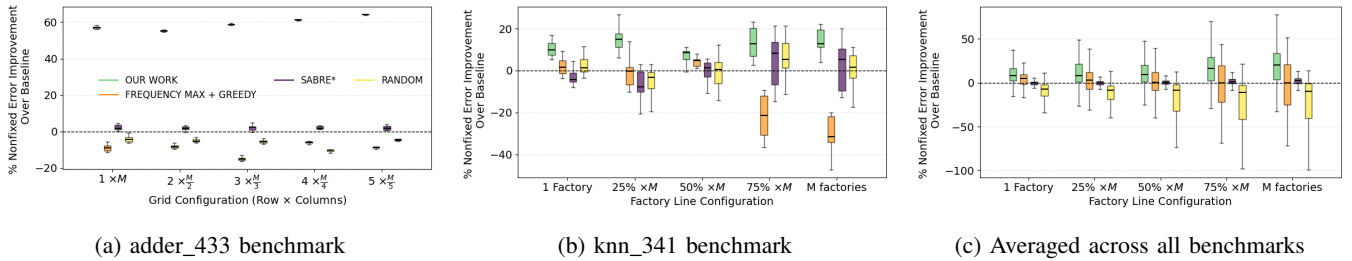


Fig. 18: Factory density as a function of the number of modules, M where a factory is added at every $\lceil x\% \times M \rceil$ spots.

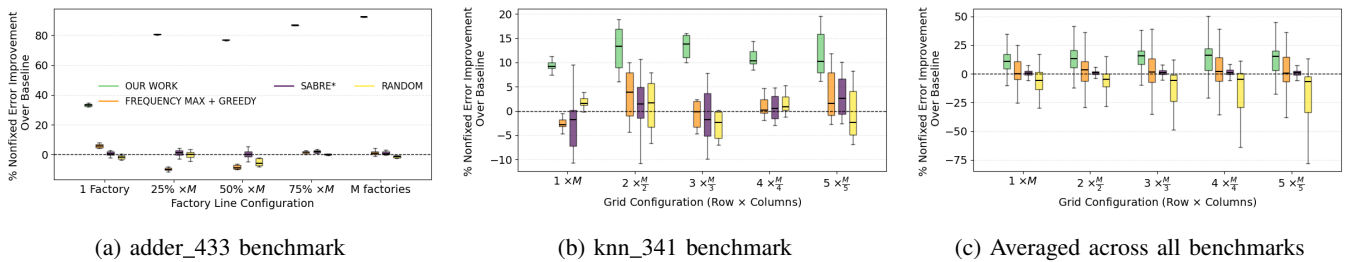


Fig. 19: Sensitivity to grid configurations where the grid is size $x \times \frac{M}{x}$ where M is the number of modules.

contributions of < 1 . The reduction in P_{error} obtained by our policy will increase as a result, thereby making our proposal robust.

2) *Sensitivity to Number of Logical Qubits per Module:* We use the gross code, i.e., the $[[144, 12, 12]]$ code, as the example code throughout the paper. However, there exist many other candidate high-rate codes, with different $[[n, k, d]]$ parameters. We evaluate the improvement in $P_{\text{non-fixed}}$ in Figure 17 on varying the number of logical qubits per module, which will be equal to $k - 1$ for a $[[n, k, d]]$ code. As k reduces, the relative improvement in $P_{\text{non-fixed}}$ by our mapper improves since fewer qubits per module increases the number of modules present in the architecture, and also increases average number of inter-module measurements needed per rotation. This indicates that as we scale quantum systems and become capable of running circuits on a larger number of modules, the improvements gained by our mapping policy will become even more relevant and substantial, whereas the improvements obtained from the baselines either reduce or remain the same.

3) *Sensitivity to Factory Placement:* We evaluate the improvements in $P_{\text{non-fixed}}$ of our mapping policy and other baselines as we allocate more factories within the architecture

in Figure 18. We start with a single factory at the top as assumed by [31], and then increase the factory allocation by spreading out $f \cdot M$ factories along the line, where f is a fraction between 25% – 100% and M is the number of modules needed by each benchmark. The performance of our policy improves as we increase the factory allocation, whereas the baselines underperform with increased factory availability. This is a result of not accounting for factory placement, and only optimizing for relative placement between modules.

4) *Sensitivity to Grid Architectures:* We also evaluate the improvement in $P_{\text{non-fixed}}$ of our mapping policy and other baselines with respect to the grid topology as described in Section IV-C. The improvements in our scheme either improve or are largely unaffected by changes to the topology. However, the greedy and NISQ baselines start underperforming as we move towards wider grids since they do not account for multiple possible placements with equivalent priorities.

VI. DISCUSSION AND CONCLUSION

The logical qubit mapping problem for the BB code is a new unexplored problem that arises in the context of spatially efficient, fault-tolerant quantum architectures. Although

it shares similarity with NISQ-era qubit mapping problem, our results demonstrate that direct adaptation of NISQ mappers is insufficient. These NISQ mappers lack the ability to adequately address the two level-nature of the problem, are unable to model arbitrary length- n interactions, and fail to distinguish between the unique clustering and assignment subproblems. To address these limitations, we introduce a mapping policy, which handles the clustering problem by modeling length- n logical qubit interactions, and addresses the assignment problem using a priority based heuristic that promotes efficient path reuse. We also prove the optimality of the assignment heuristic for a line architecture and a single factory. Across large benchmarks, Our mapper reduces the non-fixed component of program failure rate by approximately $\sim 13\%$ on average, and by $\sim 11\%$ on medium-sized benchmarks. We also find an efficient path-finding algorithm on another specific connection topology under consideration by researchers for fault tolerance, the “long grid”. Our proposal maintains strong performance across topologies achieving an average improvement of $\sim 17\%$ in non-fixed error relative to the baseline, demonstrating its robustness to architectural variation.

Overall, our results indicate that we enables substantial “free” improvements in program failure rate ($\sim 4\%$, which further improves to $\sim 10.5\%$ as factory error rates will get better) without requiring any hardware modifications. This alleviates part of the burden on hardware designers and provides a promising software-level pathway toward early FTQC.

ACKNOWLEDGEMENTS

We would like to thank Patrick Rall and Eddie Schoute for their discussions and valuable inputs related to the tour de gross architecture [31]. This work was funded in part by NSF 24-599: Quantum Leap Challenge Institutes (QLCI) and by the NSF STAQ project (PHY-2325080).

REFERENCES

[1] R. Acharya, D. A. Abanin, L. Aghababaie-Beni, I. Aleiner, T. I. Andersen, M. Ansmann, F. Arute, K. Arya, A. Asfaw, N. Astrakhantsev, J. Atalaya, R. Babbush, D. Bacon, B. Ballard, J. C. Bardin, J. Bausch, A. Bengtsson, A. Bilmes, S. Blackwell, S. Boixo, G. Bortoli, A. Bourassa, J. Bovaird, L. Brill, M. Broughton, D. A. Browne, B. Buchea, B. B. Buckley, D. A. Buell, T. Burger, B. Burkett, N. Bushnell, A. Cabrera, J. Campero, H.-S. Chang, Y. Chen, Z. Chen, B. Chiaro, D. Chik, C. Chou, J. Claes, A. Y. Cleland, J. Cogan, R. Collins, P. Conner, W. Courtney, A. L. Crook, B. Curtin, S. Das, A. Davies, L. De Lorenzo, D. M. Debroy, S. Demura, M. Devoret, A. Di Paolo, P. Donohoe, I. Drozdov, A. Dunsworth, C. Earle, T. Edlich, A. Eickbusch, A. M. Elbag, M. Elzouka, C. Erickson, L. Faoro, E. Farhi, V. S. Ferreira, L. F. Burgos, E. Forati, A. G. Fowler, B. Foxen, S. Ganjam, G. Garcia, R. Gasca, E. Genois, W. Giang, C. Gidney, D. Gilboa, R. Gosula, A. G. Dau, D. Graumann, A. Greene, J. A. Gross, S. Habegger, J. Hall, M. C. Hamilton, M. Hansen, M. P. Harrigan, S. D. Harrington, F. J. H. Heras, S. Heslin, P. Heu, O. Higgott, G. Hill, J. Hilton, G. Holland, S. Hong, H.-Y. Huang, A. Huff, W. J. Huggins, L. B. Ioffe, S. V. Isakov, J. Iveland, E. Jeffrey, Z. Jiang, C. Jones, S. Jordan, C. Joshi, P. Juhas, D. Kafri, H. Kang, A. H. Karamlou, K. Kechedzhi, J. Kelly, T. Khair, T. Khattar, M. Khezri, S. Kim, P. V. Klimov, A. R. Klots, B. Kobrin, P. Kohli, A. N. Korotkov, F. Kostritsa, R. Kothari, B. Kozlovskii, J. M. Kreikebaum, V. D. Kurilovich, N. Lacroix, D. Landhuis, T. Lange-Dei, B. W. Langley, P. Laptev, K.-M. Lau, L. Le Guevel, J. Ledford, J. Lee, K. Lee, Y. D.

Lensky, S. Leon, B. J. Lester, W. Y. Li, Y. Li, A. T. Lill, W. Liu, W. P. Livingston, A. Locharla, E. Lucero, D. Lundahl, A. Lunt, S. Madhuk, F. D. Malone, A. Maloney, S. Mandrà, J. Manyika, L. S. Martin, O. Martin, S. Martin, C. Maxfield, J. R. McClean, M. McEwen, S. Meeks, A. Megrant, X. Mi, K. C. Miao, A. Mieszala, R. Molavi, S. Molina, S. Montazeri, A. Morvan, R. Movassagh, W. Mruczkiewicz, O. Naaman, M. Neeley, C. Neill, N. Nersisyan, H. Neven, M. Newman, J. H. Ng, A. Nguyen, M. Nguyen, C.-H. Ni, M. Y. Niu, T. E. O'Brien, W. D. Oliver, A. Opremcak, K. Ottosson, A. Petukhov, A. Pizzuto, J. Platt, R. Potter, O. Pritchard, L. P. Pryadko, C. Quintana, G. Ramachandran, M. J. Reagor, J. Redding, D. M. Rhodes, G. Roberts, E. Rosenberg, E. Rosenfeld, P. Roushan, N. C. Rubin, N. Saei, D. Sank, K. Sankaragomathi, K. J. Satzinger, H. F. Schurkus, C. Schuster, A. W. Senior, M. J. Shearn, A. Shorter, N. Shutty, V. Shvarts, S. Singh, V. Sivak, J. Skrzynski, S. Small, V. Smelyanskiy, W. C. Smith, R. D. Somma, S. Springer, G. Sterling, D. Strain, J. Suchard, A. Szasz, A. Szein, D. Thor, A. Torres, M. M. Torunbalci, A. Vaishnav, J. Vargas, S. Vdovichev, G. Vidal, B. Villalonga, C. V. Heidweiller, S. Waltman, S. X. Wang, B. Ware, K. Weber, T. Weidel, T. White, K. Wong, B. W. K. Woo, C. Xing, Z. J. Yao, P. Yeh, B. Ying, J. Yoo, N. Yosri, G. Young, A. Zalcman, Y. Zhang, N. Zhu, and N. Zobrist, “Quantum error correction below the surface code threshold,” *Nature*, vol. 638, no. 8052, p. 920–926, Dec. 2024. [Online]. Available: <http://dx.doi.org/10.1038/s41586-024-08449-y>

[2] J. M. Baker, C. Duckering, A. Hoover, and F. T. Chong, “Time-sliced quantum circuit partitioning for modular architectures,” in *Proceedings of the 17th ACM International Conference on Computing Frontiers*, ser. CF '20. New York, NY, USA: Association for Computing Machinery, 2020, p. 98–107. [Online]. Available: <https://doi.org/10.1145/3387902.3392617>

[3] J. M. Baker, D. I. Schuster, and F. T. Chong, “Memory-equipped quantum architectures: The power of random access,” in *Proceedings of the ACM International Conference on Parallel Architectures and Compilation Techniques*, ser. PACT '20. New York, NY, USA: Association for Computing Machinery, 2020, p. 387–398. [Online]. Available: <https://doi.org/10.1145/3410463.3414644>

[4] D. Bluvstein, S. J. Evered, A. A. Geim, S. H. Li, H. Zhou, T. Manovitz, S. Ebadi, M. Cain, M. Kalinowski, D. Hangleiter, J. P. Bonilla Ataides, N. Maskara, I. Cong, X. Gao, P. Sales Rodriguez, T. Karolyshyn, G. Semeghini, M. J. Gullans, M. Greiner, V. Vuletić, and M. D. Lukin, “Logical quantum processor based on reconfigurable atom arrays,” *Nature*, vol. 626, no. 7997, p. 58–65, Dec. 2023. [Online]. Available: <http://dx.doi.org/10.1038/s41586-023-06927-3>

[5] S. Bravyi, A. W. Cross, J. M. Gambetta, D. Maslov, P. Rall, and T. J. Yoder, “High-threshold and low-overhead fault-tolerant quantum memory,” *Nature*, vol. 627, no. 8005, p. 778–782, Mar. 2024. [Online]. Available: <http://dx.doi.org/10.1038/s41586-024-07107-7>

[6] S. Bravyi, G. Smith, and J. A. Smolin, “Trading classical and quantum computational resources,” *Phys. Rev. X*, vol. 6, p. 021043, Jun 2016. [Online]. Available: <https://link.aps.org/doi/10.1103/PhysRevX.6.021043>

[7] B. J. Brown and S. Roberts, “Universal fault-tolerant measurement-based quantum computation,” *Phys. Rev. Res.*, vol. 2, p. 033305, Aug 2020. [Online]. Available: <https://link.aps.org/doi/10.1103/PhysRevResearch.2.033305>

[8] D. Castelvecchi, “Ibm releases first-ever 1,000-qubit quantum chip,” *Nature*, vol. 624, no. 7991, p. 238, 2023, news in Focus. [Online]. Available: <https://www.nature.com/articles/d41586-023-03854-1>

[9] A. M. Childs, D. Maslov, Y. Nam, N. J. Ross, and Y. Su, “Toward the first quantum simulation with quantum speedup,” *Proceedings of the National Academy of Sciences*, vol. 115, no. 38, pp. 9456–9461, sep 2018. [Online]. Available: <https://doi.org/10.1073%2Fpnas.1801723115>

[10] J. N. Eberhardt and V. Steffan, “Logical operators and fold-transversal gates of bivariate bicycle codes,” *IEEE Transactions on Information Theory*, vol. 71, no. 2, pp. 1140–1152, 2025.

[11] A. W. Harrow, A. Hassidim, and S. Lloyd, “Quantum algorithm for linear systems of equations,” *Physical Review Letters*, vol. 103, no. 15, oct 2009. [Online]. Available: <https://doi.org/10.1103%2Fphysrevlett.103.150502>

[12] Z. He, A. Cowtan, D. J. Williamson, and T. J. Yoder, “Extractors: Qldpc architectures for efficient pauli-based computation,” 2025. [Online]. Available: <https://arxiv.org/abs/2503.10390>

[13] F. Hua, Y. Chen, Y. Jin, C. Zhang, A. Hayes, Y. Zhang, and E. Z. Zhang, “Autobraid: A framework for enabling efficient surface code

- communication in quantum computing,” in *MICRO-54: 54th Annual IEEE/ACM International Symposium on Microarchitecture*, ser. MICRO '21. New York, NY, USA: Association for Computing Machinery, 2021, p. 925–936. [Online]. Available: <https://doi.org/10.1145/3466752.3480072>
- [14] I. D. Kivlichan, C. Gidney, D. W. Berry, N. Wiebe, J. McClean, W. Sun, Z. Jiang, N. Rubin, A. Fowler, A. Aspuru-Guzik, H. Neven, and R. Babbush, “Improved fault-tolerant quantum simulation of condensed-phase correlated electrons via trotterization,” *Quantum*, vol. 4, p. 296, jul 2020. [Online]. Available: <https://doi.org/10.22331/q-2020-07-16-296>
- [15] A. Li, S. Stein, S. Krishnamoorthy, and J. Ang, “Qasmbench: A low-level quantum benchmark suite for nisq evaluation and simulation,” *ACM Transactions on Quantum Computing*, vol. 4, no. 2, Feb. 2023. [Online]. Available: <https://doi.org/10.1145/3550488>
- [16] G. Li, Y. Ding, and Y. Xie, “Tackling the qubit mapping problem for nisq-era quantum devices,” in *Proceedings of the Twenty-Fourth International Conference on Architectural Support for Programming Languages and Operating Systems*, ser. ASPLOS '19. New York, NY, USA: Association for Computing Machinery, 2019, p. 1001–1014. [Online]. Available: <https://doi.org/10.1145/3297858.3304023>
- [17] D. Litinski, “A game of surface codes: Large-scale quantum computing with lattice surgery,” *Quantum*, vol. 3, p. 128, 2019.
- [18] R. Mandelbaum, J. Gambetta, J. Chow, T. Mittal, T. J. Yoder, A. Cross, and M. Steffen, “How IBM will build the world’s first large-scale, fault-tolerant quantum computer,” *IBM Quantum Blog*, 6 2025, accessed: 2025-11-18. [Online]. Available: <https://www.ibm.com/quantum/blog/large-scale-ftqc>
- [19] H. J. Manetsch, G. Nomura, E. Bataille, X. Lv, K. H. Leung, and M. Endres, “A tweezer array with 6,100 highly coherent atomic qubits,” *Nature*, vol. 647, no. 8088, p. 60–67, Sep. 2025. [Online]. Available: <http://dx.doi.org/10.1038/s41586-025-09641-4>
- [20] A. Molavi, A. Xu, M. Diges, L. Pick, S. Tannu, and A. Albarghouthi, “Qubit mapping and routing via maxsat,” 2022. [Online]. Available: <https://arxiv.org/abs/2208.13679>
- [21] L. Pause, L. Sturm, M. Mittenbühler, S. Amann, T. Preuschoff, D. Schäffner, M. Schlosser, and G. Birkl, “Supercharged two-dimensional tweezer array with more than 1000 atomic qubits,” *Optica*, vol. 11, no. 2, p. 222, Feb. 2024. [Online]. Available: <http://dx.doi.org/10.1364/OPTICA.513551>
- [22] R. Raussendorf and H. J. Briegel, “A one-way quantum computer,” *Phys. Rev. Lett.*, vol. 86, pp. 5188–5191, May 2001. [Online]. Available: <https://link.aps.org/doi/10.1103/PhysRevLett.86.5188>
- [23] B. W. Reichardt, A. Paetznic, D. Aasen, I. Basov, J. M. Bello-Rivas, P. Bonderson, R. Chao, W. van Dam, M. B. Hastings, R. V. Mishmash, A. Paz, M. P. da Silva, A. Sundaram, K. M. Svore, A. Vaschillo, Z. Wang, M. Zanner, W. B. Cairncross, C.-A. Chen, D. Crow, H. Kim, J. M. Kindem, J. King, M. McDonald, M. A. Norcia, A. Ryou, M. Stone, L. Wadleigh, K. Barnes, P. Battaglino, T. C. Bohdanowicz, G. Booth, A. Brown, M. O. Brown, K. Cassella, R. Coxe, J. M. Epstein, M. Feldkamp, C. Griger, E. Halperin, A. Heinz, F. Hummel, M. Jaffe, A. M. W. Jones, E. Kapit, K. Kotru, J. Lauigan, M. Li, J. Marjanovic, E. Megidish, M. Meredith, R. Morshead, J. A. Muniz, S. Narayanaswami, C. Nishiguchi, T. Paule, K. A. Pawlak, K. L. Pudenz, D. R. Pérez, J. Simon, A. Smull, D. Stack, M. Urbanek, R. J. M. van de Veerdonk, Z. Vendeiro, R. T. Weverka, T. Wilkason, T.-Y. Wu, X. Xie, E. Zaly-Geller, X. Zhang, and B. J. Bloom, “Fault-tolerant quantum computation with a neutral atom processor,” 2025. [Online]. Available: <https://arxiv.org/abs/2411.11822>
- [24] M. Reiher, N. Wiebe, K. M. Svore, D. Wecker, and M. Troyer, “Elucidating reaction mechanisms on quantum computers,” *Proceedings of the National Academy of Sciences*, vol. 114, no. 29, pp. 7555–7560, 2017. [Online]. Available: <https://www.pnas.org/doi/abs/10.1073/pnas.1619152114>
- [25] H. Sayginel, S. Koutsoumpas, M. Webster, A. Rajput, and D. E. Browne, “Fault-tolerant logical clifford gates from code automorphisms,” *PRX Quantum*, vol. 6, p. 030343, Sep 2025. [Online]. Available: <https://link.aps.org/doi/10.1103/vf7v-cpq9>
- [26] S. Schlag, “High-quality hypergraph partitioning,” Ph.D. dissertation, Karlsruhe Institute of Technology, Germany, 2020.
- [27] S. Schlag, T. Heuer, L. Gottesbüren, Y. Akhremtsev, C. Schulz, and P. Sanders, “High-quality hypergraph partitioning,” *ACM J. Exp. Algorithmics*, mar 2022. [Online]. Available: <https://doi.org/10.1145/3529090>
- [28] P. W. Shor, “Polynomial-time algorithms for prime factorization and discrete logarithms on a quantum computer,” *SIAM review*, 1999.
- [29] A. Silva, X. Zhang, Z. Webb, M. Kramer, C. W. Yang, X. Liu, J. Lemieux, K.-W. Chen, A. Scherer, and P. Ronagh, “Multi-qubit Lattice Surgery Scheduling,” *LIPICs, Volume 310, TQC 2024*, vol. 310, pp. 1:1–1:22, 2024, arXiv:2405.17688 [quant-ph]. [Online]. Available: <http://arxiv.org/abs/2405.17688>
- [30] Q. Xu, J. P. B. Ataiades, C. A. Pattison, N. Raveendran, D. Bluvstein, J. Wurtz, B. Vasic, M. D. Lukin, L. Jiang, and H. Zhou, “Constant-overhead fault-tolerant quantum computation with reconfigurable atom arrays,” 2023. [Online]. Available: <https://arxiv.org/abs/2308.08648>
- [31] T. J. Yoder, E. Schoute, P. Rall, E. Pritchett, J. M. Gambetta, A. W. Cross, M. Carroll, and M. E. Beverland, “Tour de gross: A modular quantum computer based on bivariate bicycle codes,” 2025. [Online]. Available: <https://arxiv.org/abs/2506.03094>
- [32] H. Zou, M. Treinish, K. Hartman, A. Ivrii, and J. Lishman, “Lightsabre: A lightweight and enhanced sabre algorithm,” 2024. [Online]. Available: <https://arxiv.org/abs/2409.08368>